

Automated thermotectonostratigraphic basin reconstruction: Viking Graben case study

L. H. RÜPKE, S. M. SCHMALHOLZ, D. W. SCHMID, and
Y. Y. PODLADCHIKOV

ABSTRACT

We present a generic algorithm for automating sedimentary basin reconstruction. Automation is achieved through the coupling of a two-dimensional thermotectonostratigraphic forward model to an inverse scheme that updates the model parameters until the input stratigraphy is fitted to a desired accuracy. The forward model solves for lithospheric thinning, flexural isostasy, sediment deposition, and transient heat flow. The inverse model updates the crustal- and mantle-thinning factors and paleowater depth. Both models combined allow for automated forward modeling of the structural and thermal evolution of extensional sedimentary basins.

The potential and robustness of this method is demonstrated through a reconstruction case study of the northern Viking Graben in the North Sea. This reconstruction fits present stratigraphy, borehole temperatures, vitrinite reflectance data, and paleowater depth. The predictive power of the model is illustrated through the successful identification of possible targets along the transect, where the principal source rocks are in the oil and gas windows. These locations coincide well with known oil and gas occurrences.

The key benefits of the presented algorithm are as follows: (1) only standard input data are required, (2) crustal- and mantle-thinning factors and paleowater depth are automatically computed, and (3) sedimentary basin reconstruction is greatly facilitated and can thus be more easily integrated into basin analysis and exploration risk assessment.

AUTHORS

L. H. RÜPKE ~ *Physics of Geological Processes, Oslo University, P.O. Box 1048 Blindern, 0316 Oslo, Norway; present address: The Future Ocean, IFM-GEOMAR, Wischhofstr. 1-3, 24148 Kiel, Germany; lruepke@ifm-geomar.de*

Lars Helmuth Rüpke is a professor for sea-floor resources at the research cluster "The Future Ocean" at IFM-GEOMAR in Kiel, Germany. Before moving to Kiel, he was a senior researcher at Physics of Geological Processes at Oslo University, Norway. His present research focuses on passive margins, sedimentary basins, and fluid migration pattern through the Earth's crust.

S. M. SCHMALHOLZ ~ *Geological Institute, Leonhardstrasse 19, ETH Zurich, 8092 Zurich, Switzerland*

Stefan Markus Schmalholz is a senior researcher and lecturer at the Geological Institute of the Eidgenössische Technische Hochschule (ETH) Zurich, Switzerland. His present research focuses on folding and necking instabilities in rocks, low-frequency wave propagation in porous rocks, and numerical modeling of rock deformation. He holds a Ph.D. in natural sciences and a diploma in earth sciences both from ETH Zurich.

D. W. SCHMID ~ *Physics of Geological Processes, Oslo University, P.O. Box 1048 Blindern, 0316 Oslo, Norway*

Daniel Walter Schmid is a senior researcher and coordinator of the microstructures group at the Physics of Geological Processes at Oslo University, Norway. His present research focuses on small-scale rock deformation, coupling between chemical reactions and deformation, and the development of efficient numerical models. He holds a Ph.D. in geology from the ETH Zurich, Switzerland.

Y. Y. PODLADCHIKOV ~ *Physics of Geological Processes, Oslo University, P.O. Box 1048 Blindern, 0316 Oslo, Norway*

Yuri Y. Podladchikov is a professor at Oslo University and Physics of Geological Processes.

ACKNOWLEDGEMENTS

Thanks to Øyvind Steen, Rune Kyrkjebø, and Jan Inge Faleide for helpful discussions and data access. Thorough and constructive reviews by Dave Waltham, Dale Sawyer, David Pivnik, and Jim Pickens, as well as the editorial advice from Ernest Mancini, helped to improve the article. We also thank Statoil for support and GeoModelling Solutions for access to their basin-modeling tools.

INTRODUCTION

Sedimentary basins form in a variety of compressive to extensional tectonic settings. A classic example of a sedimentary basin-forming process is continental rifting (see Ziegler and Cloetingh, 2004, for a review). Rifting leads to thinning of the crust and subsequent isostatic compensation results in the formation of a surface depression that is filled with sediments (McKenzie, 1978). Given the right physicochemical conditions, buried organic matter undergoes chemical alteration reactions that produce hydrocarbons. These hydrocarbons may accumulate in traps to form commercially interesting reservoirs. A key to assessing a sedimentary basin's hydrocarbon prospect is therefore to understand its thermal and structural evolution.

Numerical modeling allows for the quantitative analysis of sedimentary basins. Existing basin models can be classified into reverse and forward models. Reverse models start from the present basin configuration and go back in time through the decompaction (backstripping) of individual stratigraphic layers (Watts and Ryan, 1976; Allen and Allen, 2005). By definition, reverse basin models almost separate the structural from the thermal solution because heat diffusion is not readily modeled backward in time (Lattès and Lions, 1969). This splitting of thermal and structural modeling may introduce inconsistencies into the results. Forward models start from an initial configuration prior to rifting and try, by deciphering the rifting process, to reproduce the present basin configuration (Kooi et al., 1992; Kusznir and Ziegler, 1992; Liu and Ranalli, 1998). This requires solving simultaneously for lithospheric thinning, sediment deposition and compaction, temperature, and isostatic compensation forward in time. Forward models are internally consistent, but require substantial a priori knowledge of a basin. For example, thinning factors, sedimentation rates, fault locations, and paleobathymetry have to be known. Such information is, however, commonly not available especially during the early phases of basin analysis. Repeated forward analysis with updated parameters is therefore required (Reemst and Cloetingh, 2000), which prolongs the time required to complete a reconstruction and limits the applicability of forward models.

This study demonstrates how the update of model parameters can be automated. The algorithm we present is based on the coupling of a forward model to an inverse scheme and does not require any a priori information on paleobathymetry, fault locations, and thinning factors. The forward model accounts for sediment deposition, blanketing, and compaction, as well as flexural isostasy, multiple thinning events of finite duration, thermal advection and conduction, and radiogenic heat production. The model resolves simultaneously for lithosphere processes (e.g., thinning, flexure, and temperature) and sedimentary basin processes (e.g., sedimentation, compaction, and maturation). The inverse algorithm automatically updates crustal- and mantle-thinning factors and paleowater depth until the input stratigraphy is fitted to a desired accuracy.

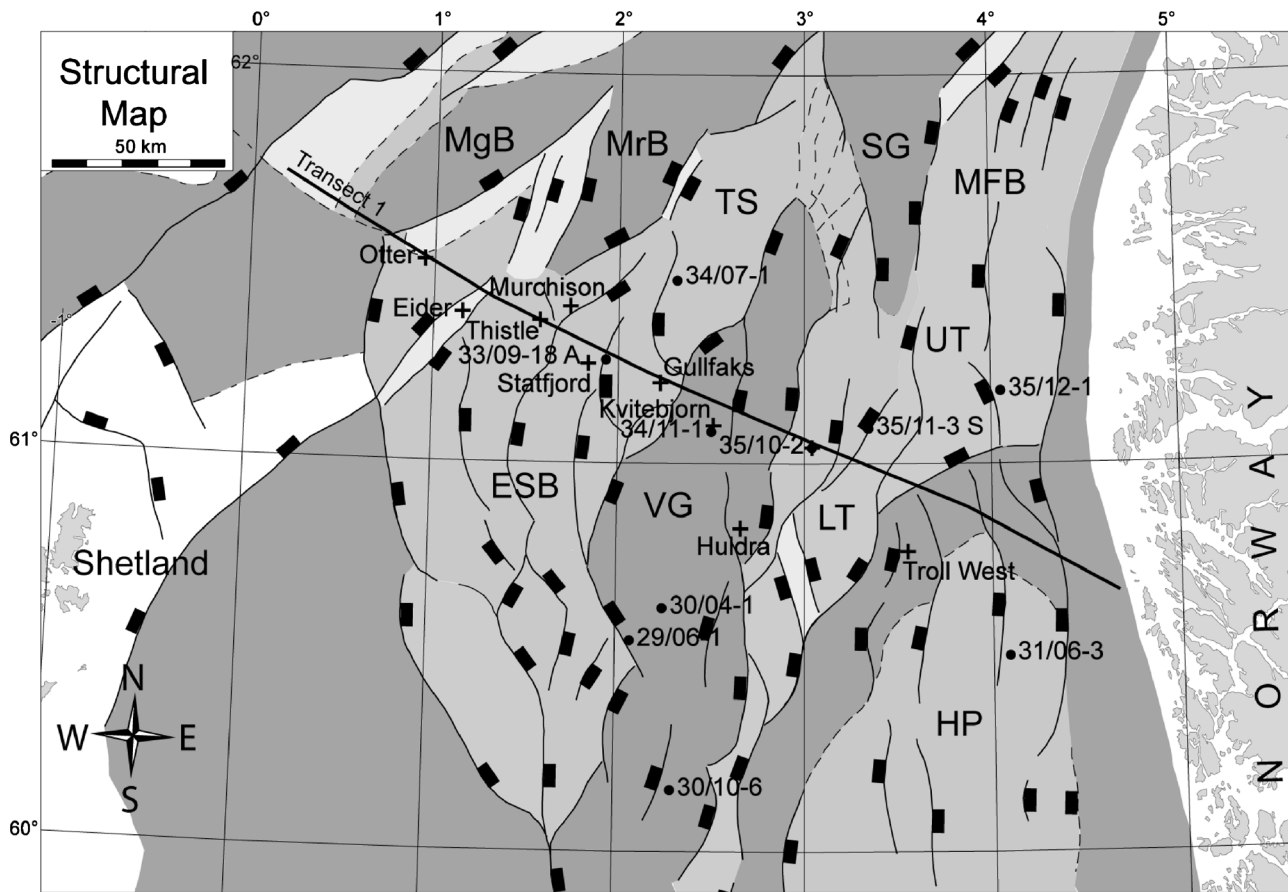


Figure 1. Location of the modeled transect 1 and structural map of the Viking Graben (modified from Faleide et al., 2002). Key wells are marked by filled circles, and some oil and gas fields in the area are marked by crosses. ESB = East Shetland Basin; HP = Horda platform; LT = Lomre terrace; MFB = Maloy fault blocks; MgB = Magnus Basin; MrB = Marulk Basin; SG = Sogn Graben; TS = Tampen Spur; UT = Uer terrace; VG = Viking Graben.

Several previous studies have addressed automated basin modeling. Poplavskii et al. (2001) presented a detailed mathematical framework for automating the parameter update of two-dimensional (2-D) forward basin models. We mostly follow the approach of Poplavskii et al. (2001) and present a modified version of it coupled to a novel forward model. Pioneering work on the inversion of stratigraphic data for lithosphere deformation has been done by White (1993, 1994). In addition, White and Bellingham (2002) presented a 2-D model for the inverse modeling of sedimentary basins.

We demonstrate the benefits and robustness of our approach through the automated reconstruction of the northern Viking Graben (Figure 1). The reconstruction is tested and quality checked against the input stratigraphy, independent paleowater depth estimates, well temperatures, and vitrinite reflectance (R_o). As a final check of the solution and to demonstrate the model's predictive power, we identify possible targets where

the dominant source rock is in the oil and gas windows. These locations coincide well with known oil and gas occurrences in the northern Viking Graben.

AUTOMATED THERMOTECTONOSTRATIGRAPHIC RECONSTRUCTION METHOD

Forward Model

We use a 2-D forward model that is locally based on pure shear kinematics (McKenzie, 1978; Kooi et al., 1992; Liu and Ranalli, 1998), allows for multiple rifting events of finite duration (Jarvis and McKenzie, 1980; Reemst and Cloetingh, 2000), and enables depth-dependent stretching (Royden and Keen, 1980; Hellinger, 1983). Along the horizontal direction, the numerical domain is split into vertical columns. Each column is assigned a crustal- (δ) and mantle (β)-thinning factor.

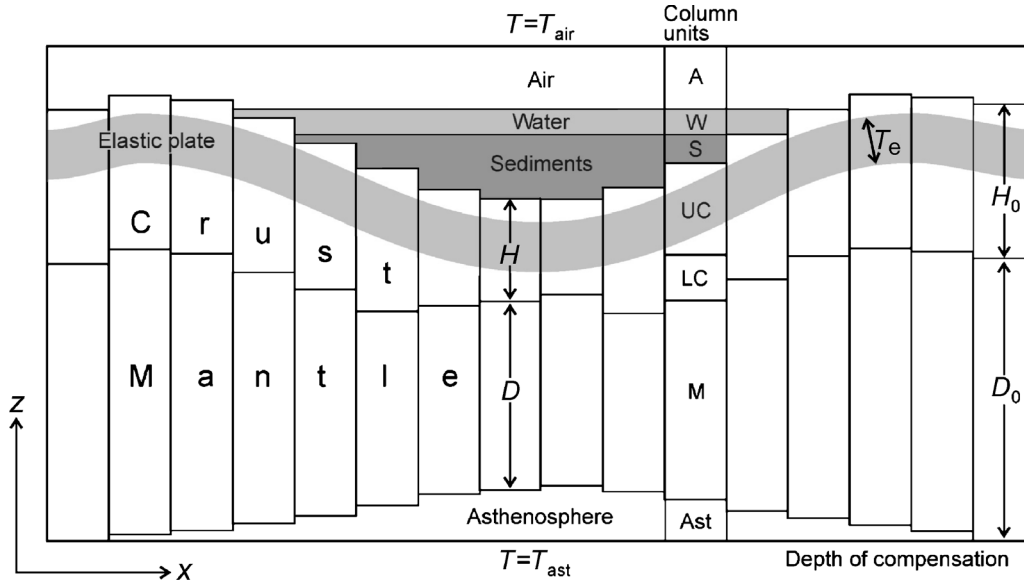


Figure 2. Model setup. The whole model domain is divided into air (A), water (W), sediments (S), upper crust (UC), lower crust (LC), lithospheric mantle (M), and asthenosphere (Ast). Thinning is defined by thinning factors that are for the crust given by the ratio H_0/H , where H_0 and H are the initial and present crustal thickness, respectively, and, for the lithospheric mantle, by the ratio D_0/D , where D_0 and D are the initial and present lithospheric mantle thickness, respectively. Variations of vertical loads resulting from both thinning and temperature changes are projected onto an elastic plate, whose flexural rigidity depends on the effective elastic thickness, T_e . T_{air} = temperature boundary condition top; T_{ast} = temperature boundary condition bottom. See text for details.

Along the vertical direction, the numerical domain is subdivided into seven major units: air, water, sediments, upper crust, lower crust, lithospheric mantle, and asthenosphere (Figure 2). Sediments can further be subdivided into subunits to discriminate between rock types. The numerical grid is deformed using an arbitrary Eulerian-Lagrangian approach (Fullsack, 1995), where the grid is moved horizontally according to crustal thinning only and is fixed in the vertical direction. The vertical and horizontal crustal velocities (v_z and v_x , respectively) for a given time step are related to the thinning factors at the specified point:

$$v_z = -\Delta z \dot{\epsilon} = -\frac{\Delta z \ln(\delta)}{\Delta t}, \quad v_x = \Delta x \dot{\epsilon} = \frac{\Delta x \ln(\delta)}{\Delta t} \quad (1)$$

The variables Δz and Δx are the vertical and horizontal distances of the specified point from the coordinate origin, respectively; $\dot{\epsilon}$ is the pure shear strain rate; and Δt is the incremental time step. Each rifting phase is assigned a total thinning factor, which is reached through several incremental thinning steps.

The vertical grid spacing is nonuniform, and the highest resolution is in the sediments and the upper parts of the crust. In the horizontal direction, the initial column width is variable, so that after stretching,

all columns have identical width. By this method, the highest numerical resolution is in those domains that experience the largest deformation. The model further includes the effects of flexural isostasy and depth of necking (Watts et al., 1982; Braun and Beaumont, 1989; Watts and Tenbrink, 1989; Weissel and Karner, 1989; Kooi et al., 1992; Kuszniir and Ziegler, 1992). The equation describing the vertical deflection of the top of the crust, w , caused by flexural isostasy is

$$\frac{\partial^2}{\partial x^2} \left(D \frac{\partial^2 w}{\partial x^2} \right) + (\rho_m - \rho_{in})g(w + S) = q \quad (2)$$

where x , D , ρ_m , ρ_{in} , g , and S are the horizontal coordinate, the flexural rigidity, the average density of the lithospheric mantle, the average density of the basin infill (compacted sediments), the acceleration caused by gravity, and the kinematic deflection caused by necking, respectively. The differential load, q , represents the differences in load relative to the load in the equilibrium state, here caused mainly by temperature-driven density changes. The flexural rigidity (D) is a cubic function of the effective elastic thickness (T_e), which is either constant or determined by the depth of a specified isotherm (Watts et al., 1982). The kinematic deflection,

S , i.e., the surface depression that results from stretching and not from isostatic compensation, is calculated using the crustal-thinning factors and the depth of necking (Kooi et al., 1992). Both ends of the elastic beam are matched to the analytical solution of a beam clamped at infinity. This permits us to solve the flexure equation only in the domain where stratigraphic data exist. The velocity field derived from pure shear kinematics and crustal flexure is used to advect the temperature field. The time-dependent heat-transport equation is solved in the entire modeling domain. The evolution of temperature, T , at one grid point is given by

$$\rho_i c_{pi} \left(\frac{\partial T}{\partial t} + v_x \frac{\partial T}{\partial x} + v_z \frac{\partial T}{\partial z} \right) = \frac{\partial}{\partial x} \left(k_i \frac{\partial T}{\partial x} \right) + \frac{\partial}{\partial z} \left(k_i \frac{\partial T}{\partial z} \right) + A_i \quad (3)$$

where i is a local material index, t is the time, and v_x and v_z are the velocities in the horizontal x and vertical z direction, respectively. Because the numerical grid is moved horizontally with the velocities resulting from crustal thinning, the horizontal velocity used in equation 3 is the differential velocity between the crust and the lithospheric mantle, which results from depth-dependent stretching. The variables ρ_i , c_{pi} , k_i , and A_i are density, specific heat, thermal conductivity, and radiogenic heat production rate, respectively. The thermal conductivity of sediments at a point is an effective material property that results from the geometric averaging of the local matrix and pore-fluid conductivities (k_m and k_w , respectively) (Woodside and Messmer, 1961; Deming and Chapman, 1989):

$$k = k_m^{(1-\phi)} k_w^{(\phi)} \quad (4)$$

where ϕ is porosity. Temperature dependence of thermal conductivity is accounted for by assuming the following relations (Deming and Chapman, 1989; Beardsmore and Cull, 2001):

$$\begin{aligned} k_w &= b_2 T^2 + b_1 T + b_0 \\ k_m &= k_m^0 \exp\left(\frac{b_f}{T} - \frac{b_f}{T_0}\right) \end{aligned} \quad (5)$$

Refer to Table 1 for parameter description. Radiogenic heat production in the crust decreases exponentially with depth (Jaupart et al., 1981; Turcotte and Schubert, 1982) and is assumed constant in the sediments. Water and sediments are incorporated in the

Table 1. Complete List of Symbols Used in the Model Formulation

Parameter	Description	Value	Units
D_o	Initial mantle thickness	93.0	km
H_o	Initial crustal thickness	32.0	km
N	Necking level	15.0	km
T_{ast}	Temperature boundary condition bottom	1573.0	K
T_{air}	Temperature boundary condition top	281.0	K
T_e	Effective elastic thickness	5.0	km
A	Radiogenic heat production	cf. Table 2	W/m ³
D	Flexural rigidity		
H	Crustal thickness		m
dL	Misfit between modeled and given horizon		m
S	Kinematic deflection		m
T	Temperature		K
b_0	Parameter in pore-fluid thermal conductivity	0.565	W/m/K
b_1	Parameter in pore-fluid thermal conductivity	1.88×10^{-3}	W/m/K ²
b_2	Parameter in pore-fluid thermal conductivity	-7.23×10^{-6}	W/m/K ³
b_f	Parameter in grain thermal conductivity	250	K
c	Compaction length scale	cf. Table 2	1/km
c_p	Specific heat	cf. Table 2	J/kg/K
d	Isostasy factor		
g	Gravitational acceleration		m/s ²
k	Thermal conductivity	cf. Table 2	W/m/K
q	Differential load		
t	Time		s
v_x, v_y	Velocity		m/s
w	Vertical deflection of the crust		m
x	Horizontal coordinate		m
z	Vertical coordinate		m
α	Thermal expansion	cf. Table 2	1/K
β	Mantle stretching factor		
δ	Crustal stretching factor		
ρ	Density	cf. Table 2	kg/m ³

thermal solver to include the effects of sediment blanketing (Debremaecker, 1983; Lucazeau and Ledouaran, 1985; Zhang, 1993; Wangen, 1995; Liu and Ranalli, 1998). Sediment deposition is controlled by the time-dependent water depth that comes out of the inversion

(see section on the automated inversion method). For each time step, a local sedimentation rate is iteratively computed so that at the end of a time step, i.e., after sedimentation, compaction, isostatic compensation, and flexure, the basin is filled to the precomputed water depth. The deposited sediments are compacted using empirical compaction laws. We use variations of the compaction laws published by Royden and Keen (1980) and Sclater and Christie (1980) that have the form

$$\phi_i = \phi_i^0 \exp(-c_i z) \quad (6)$$

where ϕ is porosity, c is a compaction length scale, and z is the burial depth (see Table 1 for parameters). The nonlinear flexural response caused by compacting sediments is calculated using a Newton-Raphson iterative scheme. Equation 2 is solved using a conservative finite-difference method (Versteeg and Malalasekera, 1995). Equation 3 is solved with an implicit conservative finite-difference method. Thereby, diffusion and heat production are calculated using the fractional step method, and advection is calculated using the method of characteristics (Versteeg and Malalasekera, 1995; Tannehill et al., 1997). The boundary conditions for the thermal solver are fixed temperatures at the base and top of the numerical domain and zero horizontal heat flow at the sides (Figure 2). Density changes, which affect the differential load, q , in equation 2 are computed from a reference density and the thermal expansion factor (McKenzie, 1978). The forward model was successfully tested versus analytical solutions for tectonic and thermal subsidence for the deflection of an elastic plate and for steady-state heat flow, including radioactive heat production rates that decay exponentially with depth.

Automated Inversion Methods

Automated reconstruction of sedimentary basins can be treated as a constrained optimization problem (Fletcher, 2000). The goal function to be minimized is the misfit between observed and modeled stratigraphic data, and additional constraints can be imposed (e.g., finite rifting durations and maximum stretching factors). The inversion consists of the iterative search for the optimal set of δ , β , and paleowater depth values, which minimize the chosen goal function (Poplavskii et al., 2001; White and Bellingham, 2002). The first iterative forward run requires an initial guess for δ , β , and paleowater depth. The

initial guess for the thinning factors is based on analytical solutions for isostasy and thermal subsidence. The initial guess for paleowater depth is based on the present water depth.

After every forward run, the misfit between the input and computed stratigraphy is used to update the δ and β factors and paleowater depth. For example, for each rifting event, the misfit for one particular stratigraphic horizon (normally, the horizon that represents the onset of the particular rifting event) is used to update the δ factors corresponding to a particular rifting event. The update rule for δ for a given column and rifting event, r , has the form

$$\delta_r^{\text{new}} = \delta_r^{\text{old}} / \left(1 + \frac{u_\delta \Delta L_r}{\lambda} \right) \quad (7)$$

where δ_r^{new} and δ_r^{old} are the new and old δ factors, respectively; u_δ is a weighting factor; ΔL_r is the depth difference between the modeled and given stratigraphic horizon that was chosen to fit rifting event r ; and λ is an isostasy factor given by

$$\lambda = \frac{\rho_m - \rho_c}{\rho_m - \rho_{in}} H \quad (8)$$

with ρ_c being the density of the crust, and H the crustal thickness. Similar update rules are defined for the β factors and paleowater depth.

Updating the δ and β factors and paleowater depth with the same weighting can cause oscillations during the inversion algorithm. Each update rule includes, therefore, a weighting coefficient such as u_δ , which ranges between 0 and 1. Normally, the biggest weight (0.7–1) is assigned to the δ factor update, the intermediate weight (0.2–0.7) is assigned to the β factor update, and the smallest weight (0–0.2) is assigned to the water depth update. The weighting of the update rules results in a stable inversion algorithm with a rapid convergence rate and reduces the required number of iterative steps (commonly less than 20). The inversion algorithm was tested successfully for robustness and correctness with synthetic stratigraphies, including tests with random noise.

Maturity Modeling

One major application of basin modeling is to quantify the thermal history of a basin to make predictions on the hydrocarbon prospect. Hydrocarbons are formed

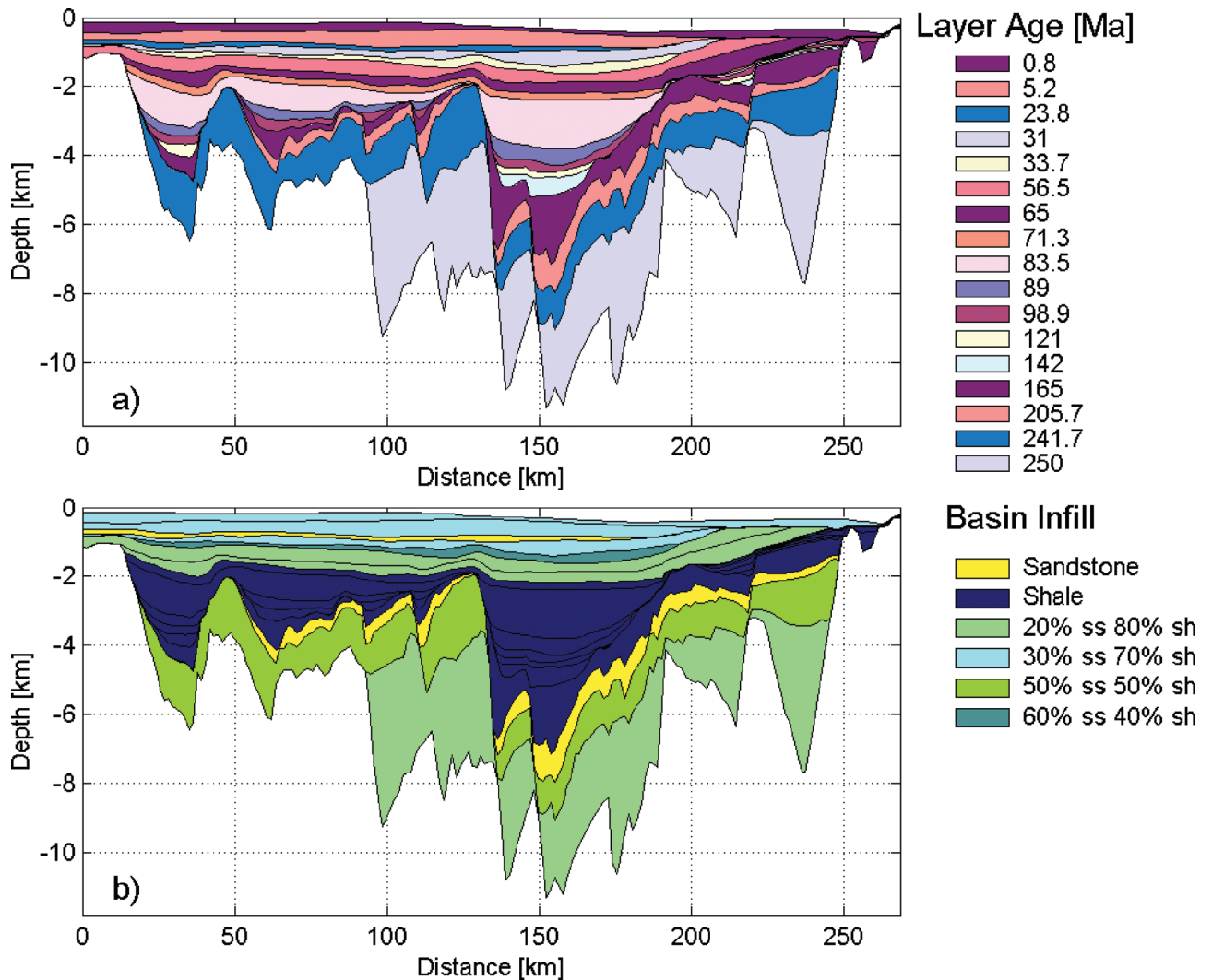


Figure 3. The upper panel plot shows the input stratigraphy. The lower panel plot shows the basin infill; ss = sandstone; sh = shale. The rock properties for individual stratigraphic layers are listed in Table 2.

during chemical alteration processes of organic matter during which volatiles, liquids, and oils are produced. The degree to which these alteration processes have progressed is commonly termed “thermal maturity.” Thermal maturity records the entire thermal history because chemical reactions are sensitive to duration and temperature. A popular proxy for paleotemperatures and thermal maturity is the R_o . In basin modeling, calculating synthetic R_o can be used both as a control parameter of the integrated thermal solution and as a measure of thermal maturity. We compute R_o from the thermal solution with the EASY%Ro algorithm (Burnham and Sweeney, 1989; Sweeney and Burnham, 1990). This algorithm is based on the kinetics of 20 reference chemical reactions, but is not sensitive to the actual chemical composition of source rocks.

Perspectives and Implementation

The described mathematical model represents a new methodology for automated 2-D basin reconstruction. The algorithm is, however, not restricted to two dimensions. A one-dimensional implementation of the algorithm is straightforward, whereas a three-dimensional (3-D) version requires a few minor modifications. In particular, a dominant rifting direction has to be specified because it is no longer implicitly set by the transect orientation. First, tests of automated 3-D basin reconstruction with synthetic stratigraphies showed a similar convergence rate of the 3-D inversion algorithm as in the 2-D case.

The presented algorithm can be efficiently implemented in all standard programming languages.

Table 2. Rock Properties of the Stratigraphic Layers Shown in Figure 3*

Age (Ma)	Formations	Lithology	ϕ^{**}	c (1/km) [†]	Density (kg/m ³)	Thermal Conductivity (W/m/K)	Heat Capacity (J/kg/K)	Radiogenic Heating (W/m ³)
0–0.8	Incl. css-10	70% shale, 30% sand	0.59	0.44	2711.0	2.07	1000.0	1×10^{-6}
0.8–5.2	Incl. css-8	70% shale, 30% sand	0.59	0.44	2711.0	2.07	1000.0	1×10^{-6}
5.2–23.8	Incl. css-5	Sandstone	0.49	0.27	2690.0	4.40	1000.0	1×10^{-6}
23.8–31	Incl. css-4	70% shale, 30% sand	0.59	0.44	2711.0	2.07	1000.0	1×10^{-6}
31–33.7	Incl. css-4	40% shale, 60% sand	0.55	0.37	2702.0	2.86	1000.0	1×10^{-6}
33.7–56.5	Incl. css-2, css-3	80% shale, 20% sand	0.60	0.46	2714.0	1.86	1000.0	1×10^{-6}
56.5–65	Incl. css-1	80% shale, 20% sand	0.60	0.46	2714.0	1.86	1000.0	1×10^{-6}
65–71.3	Cretaceous	Shale	0.62	0.50	2720.0	1.50	1000.0	1×10^{-6}
71.3–83.5	Cretaceous	Shale	0.62	0.50	2720.0	1.50	1000.0	1×10^{-6}
83.5–89	Cretaceous	Shale	0.62	0.50	2720.0	1.50	1000.0	1×10^{-6}
89–98.8	Cretaceous	Shale	0.62	0.50	2720.0	1.50	1000.0	1×10^{-6}
98.8–121	Cretaceous	Shale	0.62	0.50	2720.0	1.50	1000.0	1×10^{-6}
121–142	Cretaceous	Shale	0.62	0.50	2720.0	1.50	1000.0	1×10^{-6}
142–165	Upper Jurassic (source rock)	Shale	0.62	0.50	2720.0	1.50	1000.0	1×10^{-6}
165–187	Incl. Brent sands	Sandstone	0.49	0.27	2690.0	4.40	1000.0	1×10^{-6}
187–200	Incl. Dunlin shales	80% shale, 20% sand	0.60	0.46	2714.0	1.86	1000.0	1×10^{-6}
200–206	Incl. Statfjord sands,	Sandstone	0.49	0.27	2690.0	4.40	1000.0	1×10^{-6}
206–241.7	Teist, Lomvi, Lunde	50% shale, 50% sand	0.56	0.39	2705.0	2.57	1000.0	1×10^{-6}
241.7–250	Upper Paleozoic	80% shale, 20% sand	0.60	0.46	2714.0	1.86	1000.0	1×10^{-6}

*The css sequences refer to Cenozoic Seismic Sequences as defined in Jordt et al. (1995).

**Porosity.

[†]Compaction length scale.

A commercial implementation of the algorithm, TEC-MOD2D, is available (GeoModelling Solutions, 2008).

NORTHERN VIKING GRABEN CASE STUDY

The presented algorithm is generic and can be easily applied to every extensional and flexural basin. To exemplify the workflow of our basin analysis algorithm, we have reconstructed the thermal and structural evolution of the northern Viking Graben and reevaluated its hydrocarbon prospect.

Tectonic Framework and Petroleum System

The Viking Graben is a Mesozoic rift system in the northern North Sea (Figure 1). Over the past decades, this rift system has been extensively studied, and its rifting history and crustal configuration are well described (Beach, 1985, 1986; Ziegler, 1992; Nottvedt et al., 1995). Rifting in this area postdates the Caledonian

orogenic extensional collapse and is characterized by two main rifting phases since the Devonian. A first rifting event occurred in the Permian–earliest Triassic and was followed by a period of postrift subsidence. The second rift phase occurred in the Late–Middle Jurassic to the earliest Cretaceous and was again followed by postrift subsidence. Although major tectonic activity is commonly thought to have ceased after Late Jurassic rifting, evidence exists for a third tectonic event in the Tertiary. No consensus exists on the nature of this event, but limited rifting appears possible. Rifting in the North Sea has potentially been affected by heterogeneities in the lithosphere structure inherited from a tectonic activity in the Precambrian and Caledonian (Faereth et al., 1995). The importance of pre-Permian–Triassic deformation remains, however, poorly constrained and understood.

Rifting in the Viking Graben occurred predominantly in west-east and northwest-southeast direction. We focus on a 2-D transect across the northern Viking Graben (transect I in Figure 1) that runs roughly

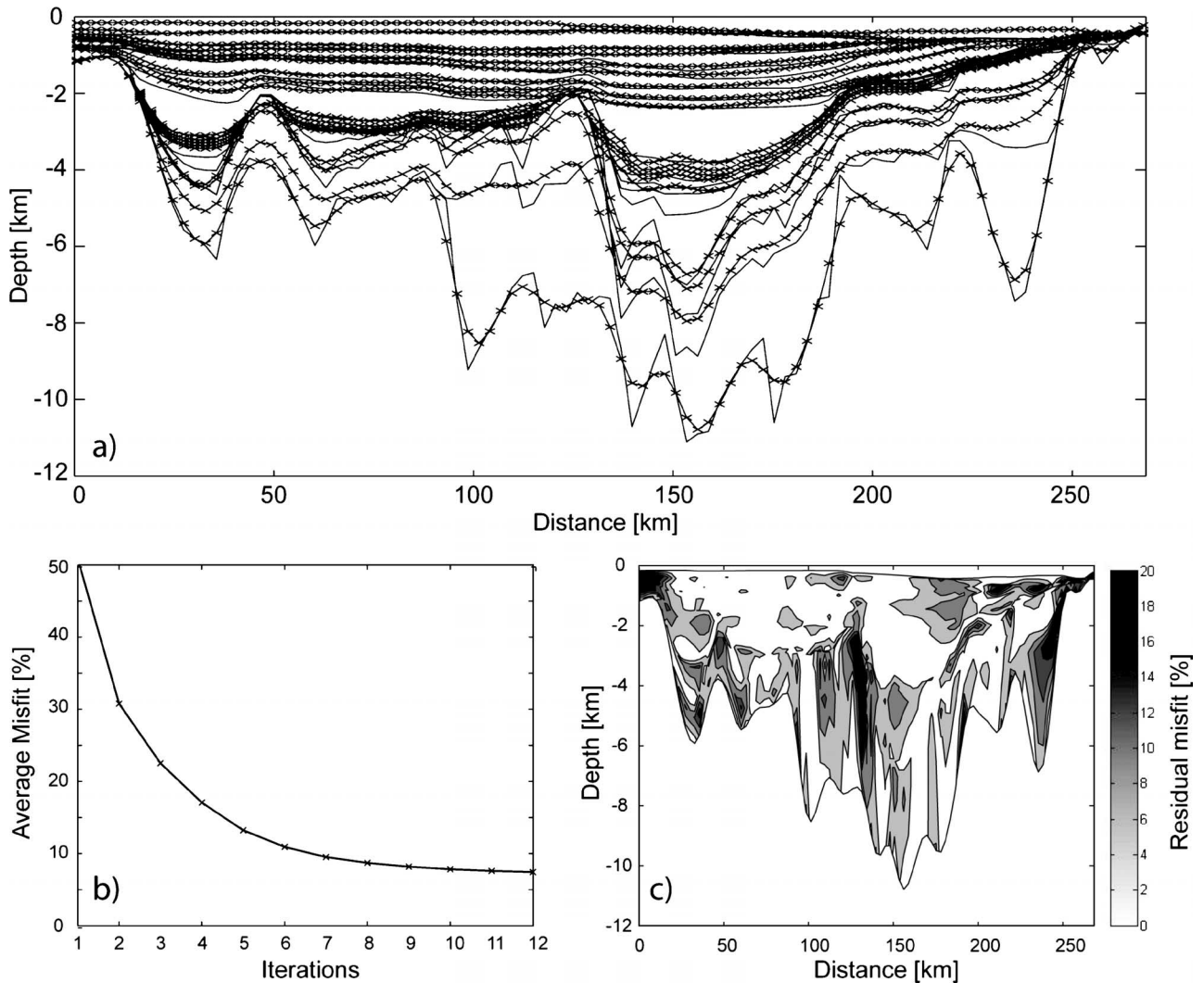


Figure 4. Results of the automatic reconstruction. Part (a) shows a comparison between the input (solid lines) and modeled (crosses) stratigraphy, (b) shows the residual average misfit for every iteration step, and (c) shows a plot of the spatial distribution of the residual misfit after the last iteration. White regions mark areas of the basin where the stratigraphy is fitted within 5% error.

parallel to the dominant rifting direction. This transect has been extensively studied (Christiansson et al., 2000; Odinsen et al., 2000; Gabrielsen et al., 2001; Faleide et al., 2002) and is well suited for 2-D analysis because of its orientation.

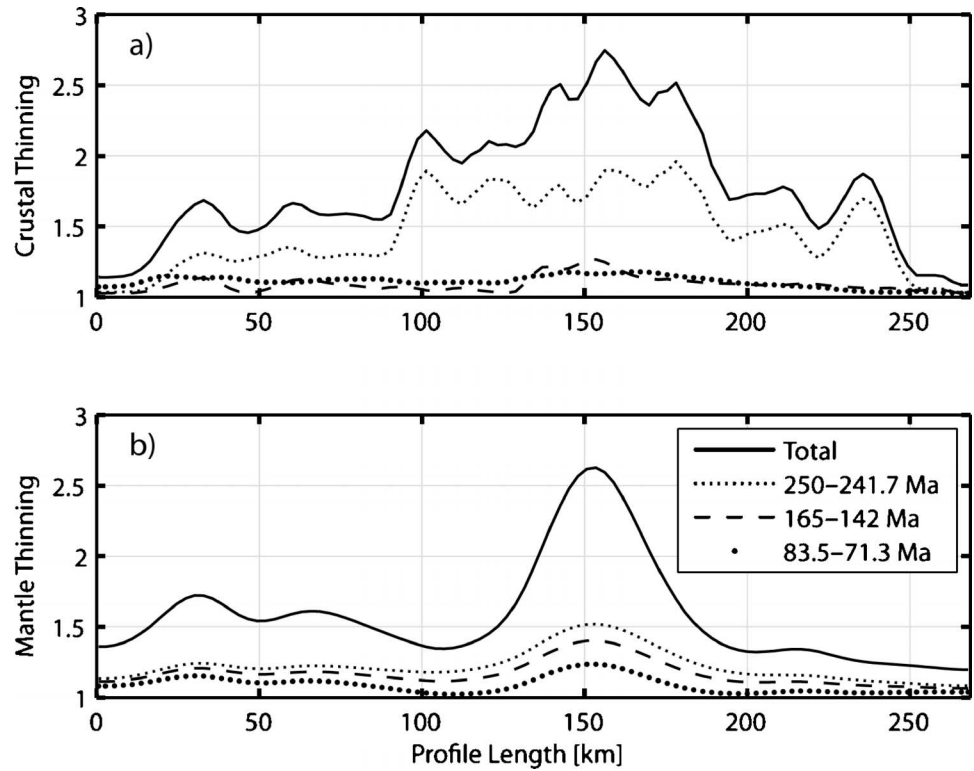
The petroleum system of the North Sea is well understood and documented in the literature (see U.S. Geological Survey report, Gautier, 2005). The Viking Graben is part of the North Sea Graben, which is one of the world's great petroleum provinces (Cornford, 1998; Gautier, 2005). Oil and gas accumulations occur in a variety of structural settings and in reservoir rocks of various ages. Practically, all hydrocarbon occurrences in this area originate from shales deposited during a short period in the Late Jurassic to the earliest Cretaceous (Kimmeridgian) (see Cornford, 1998, for a review).

Although the entire North Sea rift system shares the same source rocks, reservoir rocks vary significantly. In the northern Viking Graben, prerift Lower–Middle Jurassic sandstones are the main reservoir rocks. Sealing of traps occurs by a variety of different mechanisms. Prerift reservoirs are commonly found at tilted fault blocks where seals are formed by fine-grained postrift sedimentary sequences. Prerift reservoirs in the Viking Graben are also commonly vertically sealed through unconformable overlying shales.

Input Parameters

The input stratigraphy for the northern Viking Graben study shown in Figure 3a is color coded by the geologic age. Each stratigraphic unit (Figure 3b) has its distinct

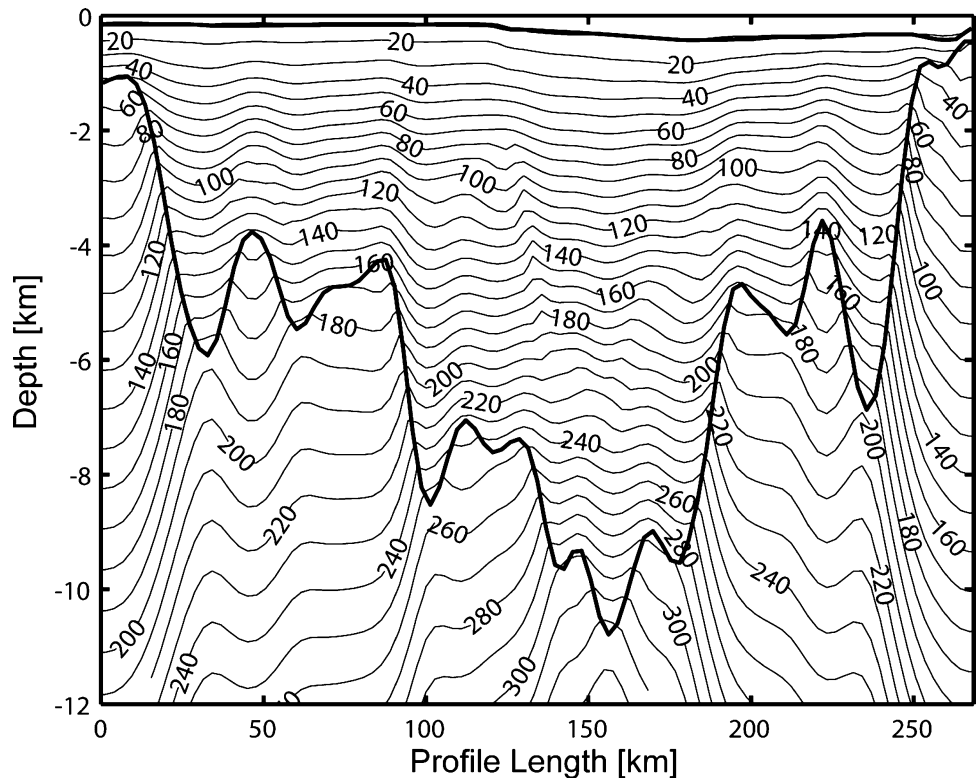
Figure 5. Computed (a) crustal- and (b) mantle thinning factors. Crustal-thinning factors are discontinuous and mimic brittle faulting. Mantle-thinning factors vary more smoothly, which is consistent with ductile flow in the hotter part of the lithosphere.



material properties and compaction laws, which are summarized in Table 2. Two to three rifting phases have been identified in the geologic record (see previous para-

graph), and we assume the following duration of the rift phases: 250–241.7, 165–142, and 83.5–71.3 Ma. As an additional input, we assume an initial crustal thickness

Figure 6. Modeled present-day temperature distribution in the sedimentary basin. Numbers on contours are temperatures in degrees Celsius. Note the lateral temperature variations that result from varying material parameters and varying basement heat flows (profile is vertically exaggerated).



of 32 km (19.88 mi), a basal lithosphere temperature of 1300°C (2372°F) at 120 km (74.56 mi) depth, and radiogenic heat production of $1 \mu\text{W}/\text{m}^3$ in the upper

continental crust and in the deposited sediments. Furthermore, we do not include any heterogeneities in the lithosphere that may have been introduced prior to the first rifting event because we have no constraints on this. The model starts therefore from an unperturbed lithosphere. The effective elastic thickness of the lithosphere is set to 5 km (3.1 mi) and the necking level to 15 km (9.3 mi). These are standard assumptions and have been demonstrated to be realistic parameter choices for the Viking Graben (Fjeldskaar et al., 2004).

Structural and Thermal Evolution

Figure 4a shows a comparison of the input stratigraphy and the modeled stratigraphy. The average residual misfit between fitted and observed horizons is approximately 7%. This fit was achieved in 12 iterations (Figure 4b). Figure 4c shows the spatial distribution of the residual error. Large parts of the basin and, in particular, the shallow sections (less than 4 km [2.5 mi]) are fitted with less than 5% error. The deeper parts of the basin are more difficult to fit, and the misfit is largest around major faults. On the average, the basin stratigraphy is fitted accurately. A closer look at the computed stretching factors shows that the crustal-thinning factors are highly variable, show abrupt variations, and mimic extensional brittle faulting (Figure 5a). Mantle-thinning factors vary more smoothly in space and are consistent with ductile deformation (Figure 5b). The maximum cumulative crustal thinning is 2.8 in the central part of the basin, which is consistent with seismic data (Christiansson et al., 2000) and previous modeling studies (Odinsen et al., 2000; Fjeldskaar et al., 2004). Mantle-thinning factors reach a maximum of 2.6 in the central part of the graben. Few observational constraints for mantle thinning are present. Nevertheless, because mantle thinning is directly related to the heat flux into the basin, thermal maturity can be used as a control parameter (see section on well control).

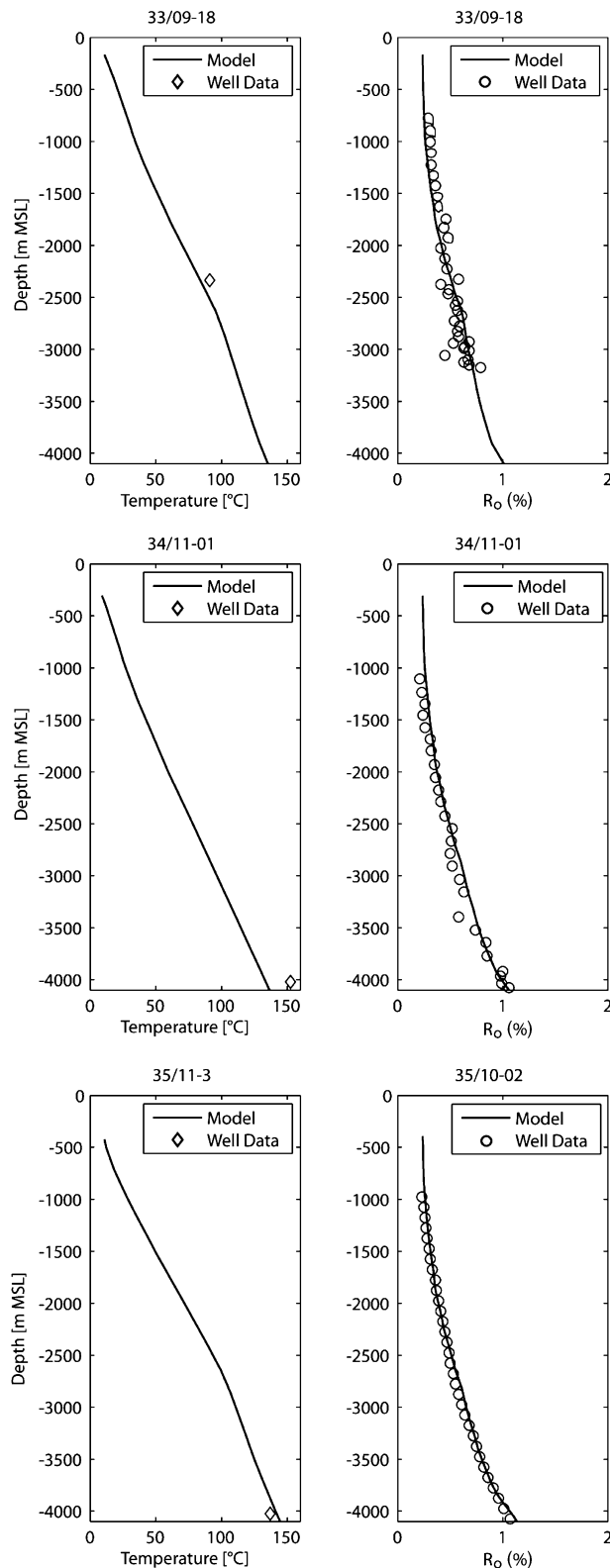


Figure 7. Well control on the thermal solution. The panel plots with diamond symbols show computed temperatures as lines and observed well temperatures as diamond symbols. The panel plots with circle symbols show computed vitrinite reflectance (R_o) as lines and observed values as circle symbols. All depths are relative to the mean sea level (MSL). The fit between computed values and measured values indicate that the reconstruction not only reproduces the present-day temperature field, but also correctly predicts the integrated heat flow, or thermal history, through time.

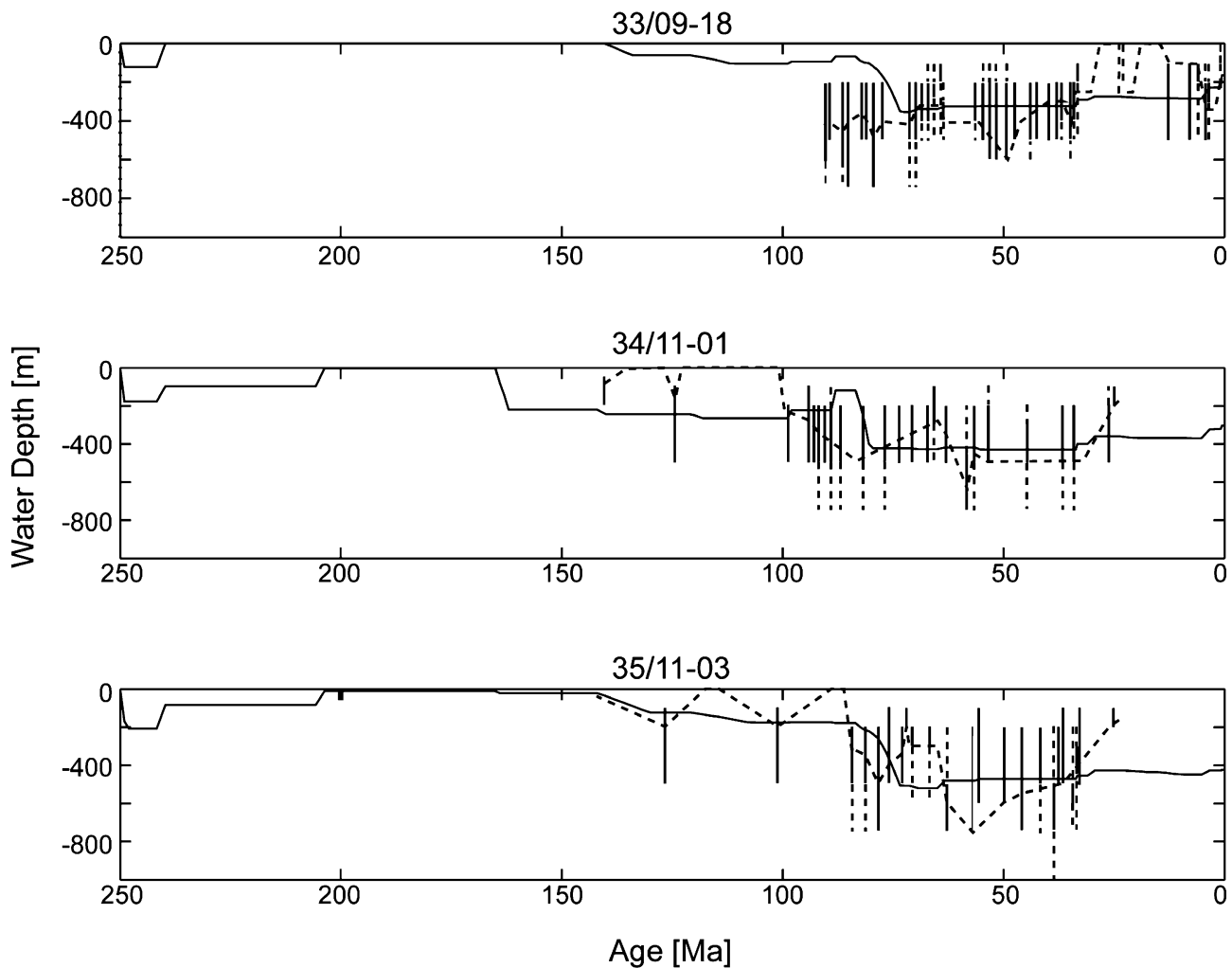


Figure 8. Paleowater depths at three well locations. The solid vertical bars are best estimates from micropaleontology. The dashed line represents the most likely trend (Kyrkjebø et al., 2001) and the solid line is the computed paleobathymetry from the inversion process.

Figure 6 shows the modeled present-day temperature distribution in the sedimentary section of the lithosphere. The present thermal gradients range between 30 and 40°C/km (1632 and 2176°F/mi), and the temperature field shows a relatively complex pattern with strong lateral temperature variations. These result from the time-dependent basement heat flow and the heterogeneity of material parameters (note that the profile is vertically exaggerated).

Well Control

Well data can be used to quality check the obtained reconstruction. We use well-log data from four wells (33/09-18 located at 119 km [73 mi], 34/11-01 located at

147 km [91.34 mi], 35/10-02 located at 177 km [109 mi], and 35/11-03 located at 191 km [118 mi] along the transect). For the wells 33/09-18 and 34/11-01, we have borehole temperature and R_o data, whereas for well 35/10-02, we have only R_o data, and for well 35/11-03, only borehole temperature data are available. As discussed above, R_o is sensitive to the integrated thermal history. A correspondence between the observed and predicted R_o indicates that the computed total heat flux through time is equal to the actual total heat flux into the basin.

Figure 7 shows a comparison of the model data and the well data. In each subplot, the left panel shows modeled temperatures with depth as a line and observed well temperatures as diamonds. At all well locations, the present temperatures are fitted very well. The

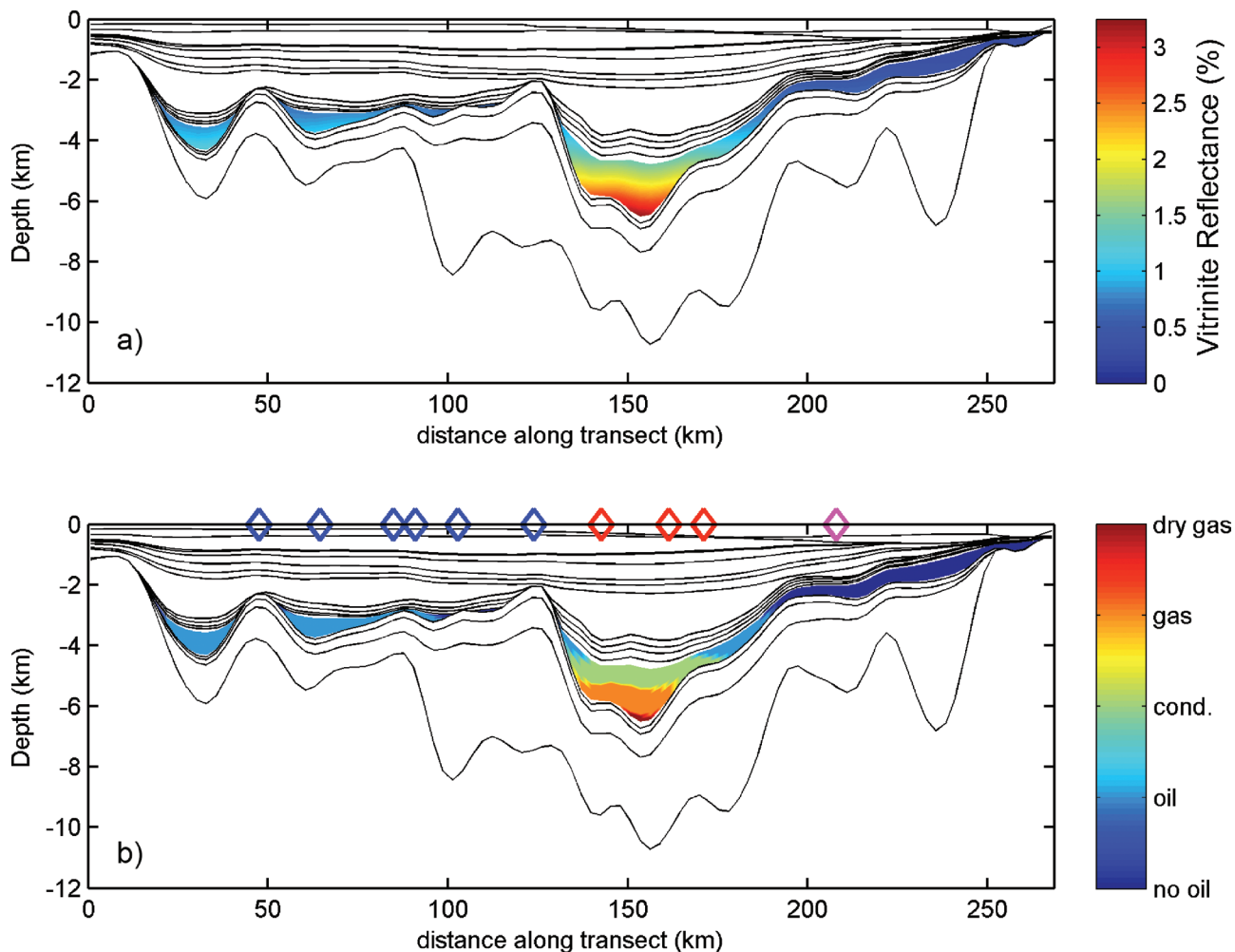


Figure 9. The upper panel plot shows computed vitrinite reflectance of Upper Jurassic sediments (deposited 161–145 Ma) that include the principal source rocks in the northern Viking Graben. Vitrinite reflectance can be translated into so-called oil and gas windows. The lower panel plot shows this translation. The reconstruction predicts oil in the western part and gas and condensates in the central part of the Graben. This fits well to the location of oil (marked by diamonds outlined in blue), gas and condensate (marked by diamonds outlined in red), and oil and gas (marked by diamonds outlined in pink) fields along the transect. The fields are, from west to east, Otter (oil), Eider (oil), Murchison (oil), Statfjord (oil), Gullfaks (oil), Kvitebjorn (gas and condensates), Huldra (gas and condensates), gas occurrences around well 35/10-2, and Troll West (oil and gas).

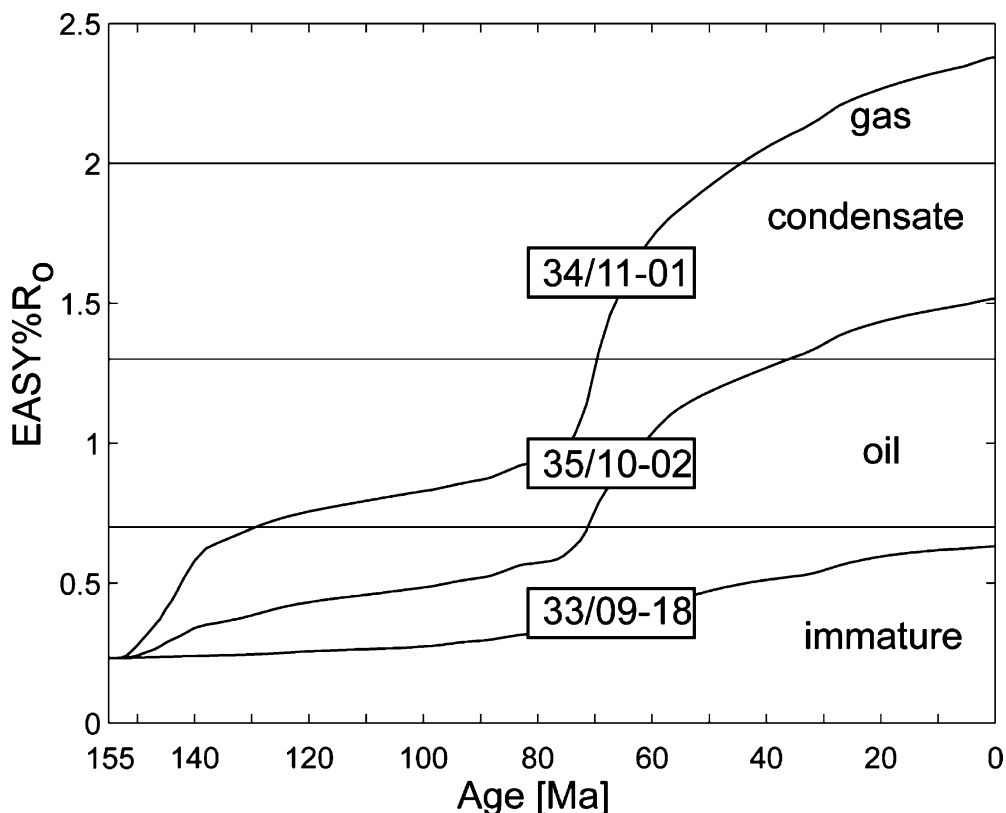
right panel plots show observed R_o as symbols and modeled R_o as lines. The computed R_o data approximates closely the observed values. This demonstrates that the model not only fits the present temperatures, but also correctly predicts the integrated heat flux through time. Another observable trait that can be used to quality check the computed structural evolution is the paleobathymetry data. Paleobathymetry is notoriously hard to constrain, but fortunately, fairly good information exists for wells 33/09-18, 34/11-01, and 35/11-03 (Kyrkjebo et al., 2001). Figure 8 shows good agreement between computed water depths and paleobathymetry information from micropaleontology.

These successful tests of the solution against various independent data sets give confidence that the reconstruction is a valid approximation of the structural and thermal evolution of the northern Viking Graben.

Implications for Hydrocarbon Maturation

Basin modeling should not only be a tool to explain data, but also have predictive power. In fact, basin models should have the ability to make predictions on the hydrocarbon prospect of a target area. To test if our model fulfills these expectations, we have identified

Figure 10. Timing of hydrocarbon maturation within Upper Jurassic sediments at wells 33/09-18, 34/11-01, and 35/10-2. The computed thermal evolution implies that the first oils were produced in the central part of the basin about 130 Ma, condensates started to form about 70 Ma, and gas about 45 Ma.



possible targets along the transect where the principal source rock is in the oil and gas windows. This is achieved by computing R_o for the principal Upper Jurassic source rocks, which is a good proxy of source rock maturity. As a rule of thumb, we assume that oil is generated from source rocks with R_o between 0.7 and 1.2%, condensates are expelled between 1.2 and 2.0%, and gas is generated for higher R_o values (Beardsmore and Cull, 2001).

Figure 9a shows the computed R_o of the Upper Jurassic source rocks, and in Figure 9b), these data are transformed into oil and gas windows. Both figures show the projected locations of known oil (marked by diamonds outlined in blue), gas and condensate (marked by diamonds outlined in red), and oil and gas (marked by diamonds outlined in pink) fields in the region. We find that our model correctly predicts oil occurrences in the western part of transect 1 and gas in the central part. It fails, however, to predict hydrocarbons in the region of the giant Troll field (pink-outlined diamond). This is explainable using the fact that no working source rock is present in this part of the graben because of erosional sand contamination from the mainland. The predictions of the model are therefore consistent with known oil and gas occurrences.

As the last test of our model, we explore the predicted history of hydrocarbon generation at the well

locations. Figure 10 shows the R_o of 155-Ma sediments (Kimmeridgian shales) versus time. The modeled thermal evolution suggests that the first oils were formed at about 130 Ma; condensates and gas started to form in the central part of the basin about 70 Ma. Farther to the west (and east), less thinning led to shallower burial of the principal source rocks and thereby to a later onset of hydrocarbon generation.

DISCUSSION

Sensitivity to Model Parameters

The presented reconstruction is consistent with most of the existing data, but unfortunately, no guarantee exists that it is correct. In fact, the solution is dependent on input parameters that are not well constrained. Two major types of uncertainties in the input data exist: (1) poorly constrained geological background data on the timing and duration of rifting, uncertainty in deposited rock types, and strength of the lithosphere and (2) poorly known effective rock properties like compaction laws and thermal properties. To test how these uncertainties affect the modeling results, we have systematically varied these input parameters in a series of

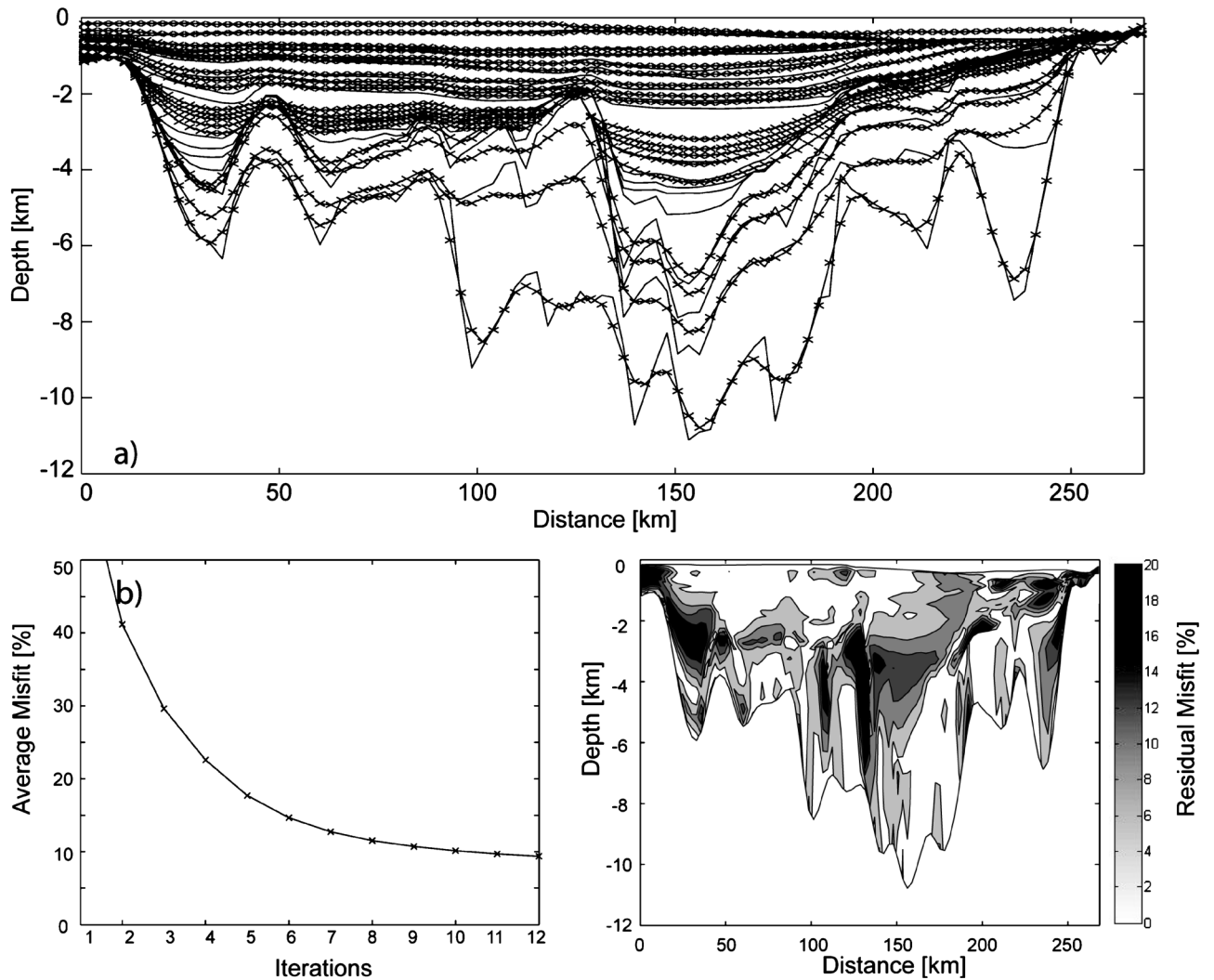


Figure 11. Results of a reconstruction that assumes only two rifting phases. The fit of the stratigraphy is slightly worse than in the case of three rifting phases. The inverse algorithm does converge well within 12 iterations and provides an acceptable reconstruction of the basin.

sensitivity tests. In particular, we have explored the differences between two and three rifting phases and the influence of variations in flexural properties.

The best fit of the input stratigraphy is achieved when assuming three rifting phases. However, the basin can also be fitted with only two rifting phases (250–241.7 and 165–142 Ma), and Figure 11 shows the results of this reconstruction. The average residual error is now about 10% instead of approximately 7% for a three-rift-phase model. The two-rift-phase model is also consistent with most of the well data (not shown), but differences become apparent when plotting time-temperature and heat flow through time (Figure 12). The three upper panel plots in Figure 12 show the vertical basement heat flow through time at the three well locations (33/09-18, 34/11-01, and 35/11-03).

Both the three- and the two-rift-phase models show synrift peaks in heat flow. The long-term decrease in heat flow, best visible at well 34/11-01, results from reduced radiogenic heating in the thinned crust. Heat flow is generally higher in the two-rift-phase model because Permian–Triassic and Jurassic rifting is more pronounced. These differences in heat flow, although never exceeding 10 mW/m^2 , result in slightly different time-temperature curves for individual stratigraphic horizons. The lower panel plots in Figure 12 show the temperature evolution of 250- and 140-Ma sediments. Temperature rapidly rises during synrift phases, whereas it increases more slowly during postrift burial.

Variations in flexural strength of the lithosphere may also affect the modeling results. The thermal implications of variations in flexural thickness and necking

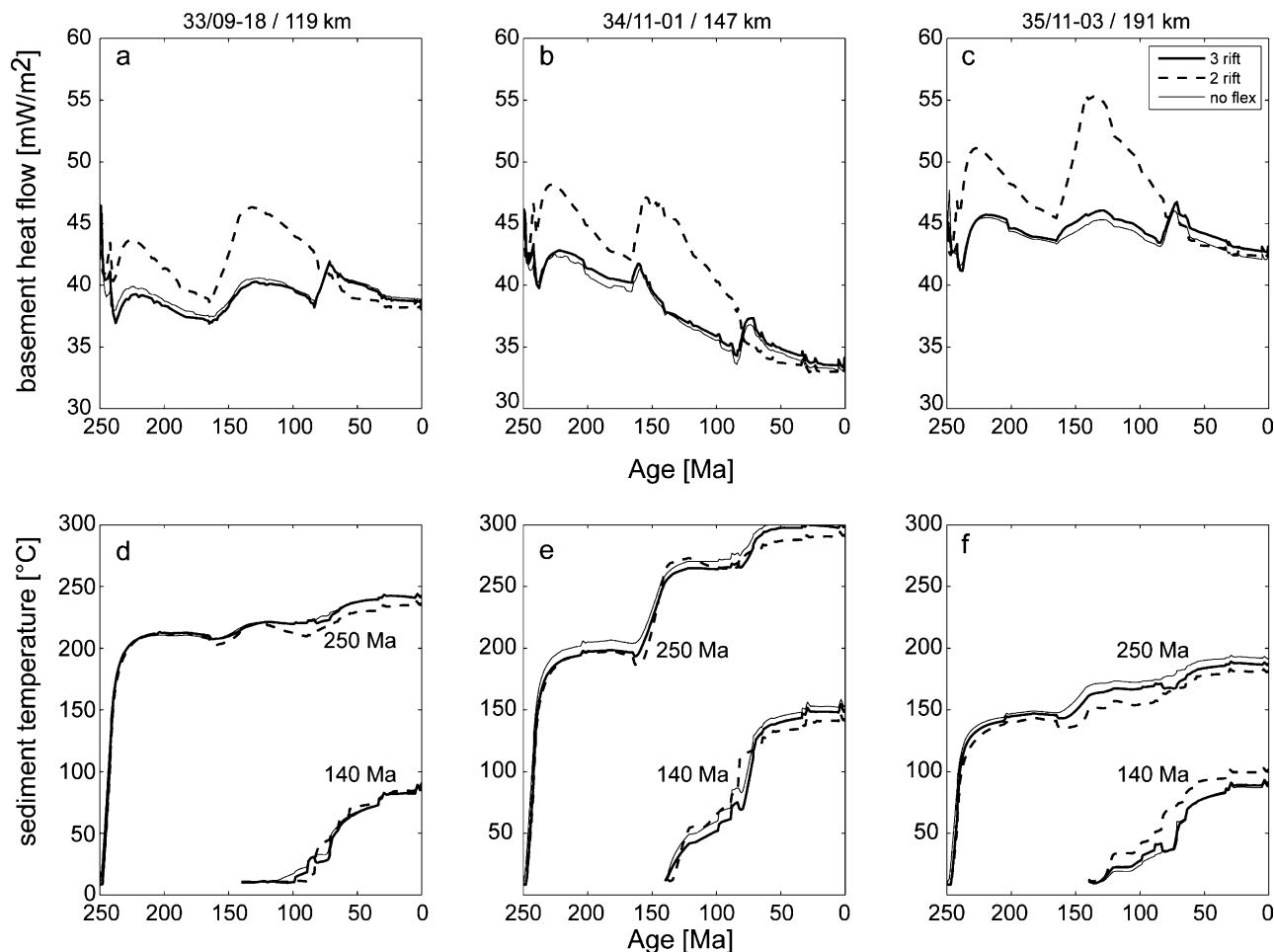


Figure 12. Sensitivity of modeling results on parameter choice. The upper panel plots show heat flow through time at three locations along the transect. The different lines correspond to a model assuming three rift phases (thick solid line), two rift phases (dashed line), and three rift phases with elastic thickness and necking level set to zero (thin solid line). The lower panel plots show time-temperature data for 250- and 140-Ma sediments for the three different models.

level are shown in Figure 12. The thin black line represents a model run with the same parameters as the three-rift-phase model, except that the elastic thickness and necking level have been set to zero. The differences between the two models are small, indicating that, in the case of the Viking Graben, the flexural properties of the lithosphere have only a secondary effect on temperature and heat flow.

Benefits and Limitations of the Algorithm

The presented case study for the northern Viking Graben demonstrates that the reconstruction of extensional basins can be mostly automated. This conclusion is consistent with the earlier works of Poplavskii et al. (2001), Bellingham and White (2002), White (1993), and White

and Bellingham (2002). Our methodology for automated basin reconstruction is, in several ways, distinct from these previous efforts.

1. We use an inverse algorithm that computes water depth through time, as well as crustal and mantle thinning during predefined rift phases, as opposed to computing a continuous strain rate distribution through time (White and Bellingham, 2002). Our approach is to predefine rift phases in accordance to the geological record. This minimizes the number of fitting parameters and mitigates nonuniqueness problems in the obtained solution. The continuous rifting scenario with an equal number of time steps and potential rift phases is an end-member case covered by the presented algorithm. Additionally, the possibility to switch off and on certain time intervals like rift events

is important to test the sensitivity of the thermal history on the number of thinning events.

2. Our forward model explicitly resolves for sedimentation, compaction, and transient heat flow.
3. The presented inversion algorithm starts from the unprocessed (not backstripped) present stratigraphy.

The main benefits of the presented methodology are a consistent structural and thermal solution that accounts for all feedback mechanisms between sedimentary and crustal processes like, e.g., sediment blanketing. Paleowater depths are inverted for and do not need to be specified a priori. The only input data required for a reconstruction are present stratigraphy and information on timing and duration of rifting. The automated reconstruction method permits to quickly run several realizations for detailed scenario analysis.

Unfortunately, the underlying inverse problem is not well posed, and its solution is nonunique: The same stratigraphy can be explained by different rift evolutions (see above). We have shown in the Viking case study that the reconstruction is consistent with well temperatures, R_o data, and paleobathymetry, although we did not include these data in the inversion. These successful blind tests indicate that we have captured the main physical processes active during rift formation.

CONCLUSIONS

We have shown that basin reconstruction can be automated. A key to this is a self-consistent forward model that accounts for the first-order physical processes of extensional basin formation and an inverse scheme that automates the model parameter update. As a real-world test, we have reconstructed the structural and thermal evolution of the northern Viking Graben.

The key findings are the following:

- Basin reconstruction can be automated and thereby facilitated.
- Using our approach of automated basin fitting, only a minimum set of standard input data is required (present stratigraphy). No a priori knowledge of thinning factors, fault locations, and paleobathymetry is necessary.
- The algorithm can be efficiently implemented, which allows to quickly perform several realization for detailed scenario analysis.
- Forward modeling provides self-consistent thermal and structural solutions. Blind testing against addi-

tional geologic and geophysical data provides insights into the reliability and quality of the solution.

- The quality-checked reconstruction of the Viking Graben was successfully used to predict regions where the source rock is in the oil and gas windows.
- The algorithm works well also for limited input data, which makes it particularly useful during the early stages of basin analysis.

REFERENCES CITED

- Allen, P. A., and J. R. Allen, 2005, *Basin analysis*: Oxford, Blackwell Publishing, 449 p.
- Beach, A., 1985, Some comments on sedimentary basin development in the northern North-Sea: *Scottish Journal of Geology*, v. 21, p. 493–512.
- Beach, A., 1986, A deep seismic-reflection profile across the northern North-Sea: *Nature*, v. 323, p. 53–55.
- Beardmore, G. R., and J. R. Cull, 2001, *Crustal heat flow*: Cambridge, Cambridge University Press, 324 p.
- Bellingham, P., and N. White, 2002, A two-dimensional inverse model for extensional sedimentary basins: 2. Application: *Journal of Geophysical Research*, v. 107, no. B10, 2260, 18 p., doi:10.1029/2001JB000174.
- Braun, J., and C. Beaumont, 1989, A physical explanation of the relation between flank uplifts and the breakup unconformity at rifted continental margins: *Geology*, v. 17, p. 760–764.
- Burnham, A. K., and J. J. Sweeney, 1989, A chemical kinetic-model of vitrinite maturation and reflectance: *Geochimica et Cosmochimica Acta*, v. 53, p. 2649–2657.
- Christiansson, P., J. I. Faleide, and A. M. Berge, 2000, Crustal structure in the northern North Sea: An integrated geophysical study, in A. Nøttvedt and B. T. Larsen, eds., *Dynamics of the Norwegian margin*: Geological Society (London) Special Publication 167, p. 15–40.
- Cornford, C., 1998, Source rocks and hydrocarbons of the North Sea, in K. W. Glennie, ed., *Petroleum geology of the North Sea: Basic concepts and recent advances*: Oxford, Blackwell Science, p. 376–462.
- Debrenaecker, J. C., 1983, Temperature, subsidence, and hydrocarbon maturation in extensional basins— A finite-element model: *AAPG Bulletin*, v. 67, p. 1410–1414.
- Deming, D., and D. S. Chapman, 1989, Thermal histories and hydrocarbon generation: Example from Utah-Wyoming thrust belt: *AAPG Bulletin*, v. 12, p. 1455–1471.
- Faerseth, R. B., R. H. Gabrielsen, and C. A. Hurich, 1995, Influence of basement in structuring of the North-Sea basin, offshore southwest Norway: *Norsk Geologisk Tidsskrift*, v. 75, p. 105–119.
- Faleide, J. I., R. Kyrkjebø, T. Kjennerud, R. H. Gabrielsen, H. Jordt, S. Fanavoll, and M. Bjerke, 2002, Tectonic impact on sedimentary processes during Cenozoic evolution of the northern North Sea and surrounding areas, in A. G. Doré, ed., *Exhumation of the North Atlantic margin: Timing, mechanisms and implications for petroleum exploration*: Geological Society (London) Special Publication 196, p. 235–269.
- Fjeldskaar, W., M. ter Voorde, H. Johansen, P. Christiansson, J. I. Faleide, and S. A. P. L. Cloetingh, 2004, Numerical simulation of rifting in the northern Viking Graben: The mutual effect of modelling parameters: *Tectonophysics*, v. 382, p. 189–212.
- Fletcher, R., 2000, *Practical methods of optimization*: Chichester, John Wiley & Sons, 450 p.

- Fullsack, P., 1995, An arbitrary Lagrangian-Eulerian formation for creeping flows and its application in tectonic models: *Geophysical Journal International*, v. 120, p. 1–23.
- Gabrielsen, R. H., R. Kyrkjebø, J. I. Faleide, W. Fjeldskaar, and T. Kjennerud, 2001, The Cretaceous post-rift basin configuration of the northern North Sea: *Petroleum Geoscience*, v. 7, p. 137–154.
- Gautier, D. L., 2005, Kimmeridgian shales total petroleum system of the North Sea graben province: *U.S. Geological Survey Bulletin*, v. 2204-C, 24 p.
- GeoModelling Solutions, 2008: <http://www.geomodsol.com> (accessed April 2005).
- Hellinger, S. J., 1983, Evolution of sedimentary basins: *AAPG Bulletin*, v. 67, p. 481–482.
- Jarvis, G. T., and D. P. McKenzie, 1980, Sedimentary basin formation with finite extension rates: *Earth and Planetary Science Letters*, v. 48, p. 42–52.
- Jaupart, C., J. Sclater, and G. Simmons, 1981, Heat flow studies: Constraints on the distribution of uranium, thorium and potassium in the continental crust: *Earth and Planetary Science Letters*, v. 52, p. 328–344.
- Jordt, H., J. I. Faleide, K. Bjørlykke, and M. T. Ibrahim, 1995, Cenozoic sequence stratigraphy of the central northern North Sea basin: Tectonic development, sediment distribution and provenance areas: *Marine and Petroleum Geology*, v. 12, p. 845–879.
- Kooi, H., S. Cloetingh, and J. Burrus, 1992, Lithospheric necking and regional isostasy at extensional basins: 1. Subsidence and gravity modeling with an application to the Gulf of Lions margin (SE France): *Journal of Geophysical Research*, v. 97, p. 17,553–17,571.
- Kuszniir, N. J., and P. A. Ziegler, 1992, The mechanics of continental extension and sedimentary basin formation—A simple-shear pure-shear flexural cantilever model: *Tectonophysics*, v. 215, p. 117–131.
- Kyrkjebø, R., T. Kjennerud, G. K. Gillmore, J. I. Faleide, and R. H. Gabrielsen, 2001, Cretaceous–Tertiary paleo-bathymetry in the northern North Sea; integration of paleo-water depth estimates obtained by structural restoration and micropaleontological analysis, *in* O. Martinsen and T. Dreyer, eds., *Sedimentary environments offshore Norway—Paleozoic to recent: Norwegian Petroleum Society Special Publication 10*, p. 321–345.
- Lattès, R., and J. Lions, 1969, *The method of quasi-reversibility: Applications to partial differential equations*: New York, American Elsevier, 388 p.
- Liu, G. J., and G. Ranalli, 1998, A finite-element algorithm for modelling the subsidence and thermal history of extensional basins: *Journal of Geodynamics*, v. 26, p. 1–25.
- Lucazeau, F., and S. Ledouaran, 1985, The blanketing effect of sediments in basins formed by extension—A numerical-model—Application to the Gulf of Lion and Viking Graben: *Earth and Planetary Science Letters*, v. 74, p. 92–102.
- McKenzie, D., 1978, Some remarks on the development of sedimentary basins: *Earth and Planetary Science Letters*, v. 40, p. 25–32.
- Nottvedt, A., R. H. Gabrielsen, and R. J. Steel, 1995, Tectonostratigraphy and sedimentary architecture of rift basins, with reference to the northern North-Sea: *Marine and Petroleum Geology*, v. 12, p. 881–901.
- Odinsen, T., P. Christiansson, R. H. Gabrielsen, J. I. Faleide, and A. M. Berge, 2000, The geometries and deep structure of the northern North Sea rift system, *in* A. Nottvedt and B. T. Larsen, eds., *Dynamics of the Norwegian margin*: Geological Society (London) Special Publication 167, p. 41–57.
- Poplavskii, K. N., Y. Y. Podladchikov, and R. A. Stephenson, 2001, Two-dimensional inverse modeling of sedimentary basin subsidence: *Journal of Geophysical Research*, v. 106, p. 6657–6671.
- Reemst, P., and S. Cloetingh, 2000, Polyphase rift evolution of the Voring margin (mid-Norway): Constraints from forward tectonostratigraphic modeling: *Tectonics*, v. 19, p. 225–240.
- Royden, L., and C. E. Keen, 1980, Rifting process and thermal evolution of the continental margin of eastern Canada determined from subsidence curves: *Earth and Planetary Science Letters*, v. 51, p. 343–361.
- Sclater, J. G., and P. A. F. Christie, 1980, Continental stretching—An explanation of the post-mid-Cretaceous subsidence of the central North-Sea basin: *Journal of Geophysical Research*, v. 85, p. 3711–3739.
- Sweeney, J., and A. Burnham, 1990, Evaluation of a simple model of vitrinite reflectance based on chemical kinetics: *AAPG Bulletin*, v. 74, p. 1559–1570.
- Tannehill, J. C., D. A. Anderson, and R. H. Pletcher, 1997, *Computational fluid mechanics and heat transfer*: Philadelphia, Taylor & Francis, 815 p.
- Turcotte, D., and G. Schubert, 1982, *Geodynamics*: New York, John Wiley & Sons, 450 p.
- Versteeg, H. K., and W. Malalasekera, 1995, *An introduction to computational fluid dynamics*: Harlow, England, Prentice Hall, 272 p.
- Wangen, M., 1995, The blanketing effect in sedimentary basins: *Basin Research*, v. 7, p. 283–298.
- Watts, A. B., and W. B. F. Ryan, 1976, Flexure of the lithosphere: *Tectonophysics*, v. 36, p. 25–44.
- Watts, A. B., and U. S. Tenbrink, 1989, Crustal structure, flexure, and subsidence history of the Hawaiian-islands: *Journal of Geophysical Research—Solid Earth and Planets*, v. 94, p. 10,473–10,500.
- Watts, A. B., G. D. Karner, and M. S. Steckler, 1982, Lithospheric flexure and the evolution of sedimentary basins: *Philosophical Transactions of the Royal Society of London Series A—Mathematical Physical and Engineering Sciences*, v. 305, p. 249–281.
- Weissel, J. K., and G. D. Karner, 1989, Flexural uplift of rift flanks due to mechanical unloading of the lithosphere during extension: *Journal of Geophysical Research—Solid Earth and Planets*, v. 94, p. 13,919–13,950.
- White, N., 1993, Recovery of strain rate variations from inversion of subsidence data: *Nature*, v. 366, p. 449–452.
- White, N., 1994, An inverse method for determining lithospheric strain rate variations on geological timescales: *Earth and Planetary Science Letters*, v. 122, p. 351–371.
- White, N., and P. Bellingham, 2002, A two-dimensional inverse model for extensional sedimentary basins: 1. Theory: *Journal of Geophysical Research*, v. 107, no. B10, 2259, 20 p., doi:10.1029/2001JB000173.
- Woodside, W., and J. H. Messmer, 1961, Thermal conductivity of porous media: I. Unconsolidated sands: *Journal of Applied Physics*, v. 32, p. 1688–1699.
- Zhang, Y. K., 1993, The thermal blanketing effect of sediments on the rate and amount of subsidence in sedimentary basins formed by extension (vol 218, pg 297, 1993): *Tectonophysics*, v. 225, p. 551.
- Ziegler, P. A., 1992, North-Sea rift system: *Tectonophysics*, v. 208, p. 55–75.
- Ziegler, P. A., and S. Cloetingh, 2004, Dynamic processes controlling evolution of rifted basins: *Earth-Science Reviews*, v. 64, p. 1–50.